Journal of South American Earth Sciences 28 (2009) 419–428

Contents lists available at ScienceDirect

Journal of South American Earth Sciences

journal homepage: www.elsevier.com/locate/jsames

Origin of melt pockets in mantle xenoliths from southern Patagonia, Argentina

Paola Aliani [a,*], Theodoros Ntaflos [b], Ernesto Bjerg [a]

[a] INGEOSUR, Departamento de Geología, Universidad Nacional del Sur – CONICET, San Juan 670, B8000ICN Bahía Blanca, Argentina
[b] Department of Lithospheric Sciences, University of Vienna, Althanstrasse 14, A-1090 Vienna, Austria

ARTICLE INFO

Keywords:
Melt pockets
Amphibole breakdown
Mineral and glass chemistry
Mass balance
Patagonia

ABSTRACT

Peridotite mantle xenoliths collected north of Gobernador Gregores, Patagonia, affected by cryptic and modal metasomatism bear melt pockets of unusually large size. Melt pockets consist of second generation olivine (ol2), clinopyroxene (cpx2) and spinel (sp2) ± relict amphibole (amph) immersed in a yellowish vesicular glass matrix. Amphibole breakdown was responsible for melt pocket generation as suggested by textural evidence and proved by consistent mass-balance calculations: amph → cpx2 + ol2 + sp2 + melt. Composition of calculated amphibole in amphibole-free melt pockets is very similar to that measured in amphibole-bearing melt pockets from the same xenolith, i.e. amphibole was consumed in the melt pocket generation process. In melt pockets devoid of relict amphibole, mass-balance calculations show remarkable differences between the calculated amphibole and the measured amphibole compositions in melt pockets from the same xenolith. The participation of minor proportions of a consumed reactant phase could be a reasonable explanation. In some samples the calculated phase proportion of glass is in excess compared to modal estimations based on backscattered electron images, probably because a portion of the generated melt was able to migrate out of the melt pockets. Compositional inhomogeneity of cpx2 and variable Ti Kd in cpx2 vs. glass in the same melt pocket reflect fast nucleation and growth and disequilibrium crystallisation, respectively. This and the difference between forsterite content in calculated equilibrium olivine and second generation olivine, suggest that mineral equilibrium was inhibited by rapid quenching of melt pockets.

1. Introduction

Mantle xenoliths carried by alkali basaltic rocks frequently show evidences of mantle metasomatism processes that took place prior to their inclusion in the host basalt. It is now well documented that infiltration and percolation of fluids and melts are responsible for the formation of hydrous phases (amphibole and/or phlogopite) in peridotitic xenoliths. Silicate glasses occur as inclusions in minerals and/or as intergranular blebs and/or as irregular patches. Silicate glass inclusions and patches in particular provide useful information about the nature of the melts and fluid phases that can influence and modify parts of the upper mantle. In recent years there have been many debates about the origin of melt pockets in mantle xenoliths. A number of authors (e.g. Neumann and Wulff-Pedersen, 1997; Coltorti et al., 1999) support the hypothesis that ephemeral metasomatic agents react with upper mantle minerals prior to their incorporation as xenoliths in host magmas. According to Yaxley and Kamenetsky (1999) and references therein, in situ melting of amphibole or clinopyroxene (plus or minus phlogopite), either in closed system or during reaction with a metasomatic fluid at low fluid/rock ratios is responsible for the generation of glassy patches prior to entrainment of the xenoliths in the host lava. Glasses in xenoliths could also be produced by adiabatic decompression melting of clinopyroxene, amphibole and phlogopite during their transport to the surface (Frey and Green, 1974).

Previous reports about mantle metasomatism affecting xenoliths from Patagonia were published by Gorring and Kay (2000), Laurora et al. (2001), Rivalenti et al. (2004a,b), Aliani et al. (2004), and Bjerg et al. (2005).

The Neogene volcanism in southern Patagonia between 46.5° and 49.5°S, east of the Andes, comprise voluminous late Miocene to early Pliocene tholeiitic lavas and, to a lesser extent, latest Miocene to Plio-Pleistocene xenolith-bearing alkaline lavas. The magmatism was strongly associated with the tectonic evolution of the region and detailed descriptions and major hypothesis were presented by Ramos and Kay (1992), Gorring et al. (1997), Gorring and Kay (2001), Bjerg et al. (2005) and references therein.

Glassy patches, up to 1 cm in diameter, and intergranular glasses occur in many mantle xenoliths from southern Patagonia, north of Gobernador Gregores. These are highly unusual due to their large size and lack of alteration. The purpose of this contribution is to report results of an ongoing research project devoted to

* Corresponding author. Fax: +54 291 4595148.
E-mail address: paliani@uns.edu.ar (P. Aliani).

0895-9811/$ - see front matter © 2009 Elsevier Ltd. All rights reserved.
doi:10.1016/j.jsames.2009.04.009

the identification of the reactions that could account for melt pocket generation.

2. Geological setting

The geological evolution of the South American Plate is related to the subduction of the Nazca and Antarctic plates. South of 46°S, the Andean Cordillera can be divided in two major regions (Fig. 1): the Volcanic Arc Gap (VAG) extending to 49°S, due to the Chile Rise-Trench triple junction (Stern, 2004; Ramos, 1999); this zone is followed by the Austral Volcanic Zone (AVZ), which extends from 49°S to 53°S (Stern and Kilian, 1996).

Neogene volcanism in southern Patagonia between 46° and 49°S, east of the Andes, comprises voluminous late Miocene to early Pliocene tholeiitic lavas and, to a lesser extent, latest Miocene to Plio-Pleistocene xenolith-bearing alkaline lavas. The magmatism was strongly associated with the tectonic evolution, and three major hypotheses have been proposed for the origin of the volcanism: (a) lavas erupted in an extensional regime in a back-arc environment. Ramos and Kay (1992) argued against this hypothesis because they found no significant Neogene extension, (b) lavas are related to mantle plume activity, and (c) lavas are related to "slab windows" within the subducting plates (Gorring et al., 1997; Ramos and Kay, 1992; Cande and Leslie, 1986). The major plateau lavas occur at the Meseta Buenos Aires, Meseta de la Muerte and Meseta Central.

The studied mantle xenoliths were collected in the area of Meseta Central, at a cinder cone located approximately 200 km east of the VAG region in Santa Cruz province, Argentina.

3. Analytical methods

Major and trace element bulk rock analyses were carried out with XRF techniques (Philips 2400) and Th, U and REE were analysed by ICP-MS techniques (ELAN 6100) at the University of Vienna, Department of Lithospheric Sciences, Austria. In order to avoid matrix interferences, the elements Na, K, Ti and P were analysed with XRF as trace elements. For ICP-MS technique, about 0.1 g of each sample was dissolved in a 17 ml Savillex beaker using HNO_3 and ARISTAR (high purified) HF, then transferred to 100 ml bottles, 5 ml and made up to final weight (100 g) with distilled 2% HNO_3.

Major element compositions of the glasses and minerals were determined by a CAMECA SX100 electron microprobe using a 15 kV accelerating voltage and 20 nA beam current at the Department of Lithospheric Sciences, University of Vienna, Austria. In order to reduce alkali migration in glasses, analyses were performed using a defocused beam (beam diameter of 5–10 μm at 15 kV and 10 nA) to minimise the alkali loss. The counting time on peak was 10 s for Na and K and 20 s for all other elements. The results were checked by natural and well-defined synthetic international standards. We used two TAP, one PET and one LIF crystal. Sodium, silica and potassium were analysed simultaneously in order to avoid the loss of sodium and the increase of silica. PAP correction (Pouchou and Pichoir, 1991) was applied to the data.

Trace elements content of minerals were analysed by laser ablation inductively coupled plasma mass spectrometry at University of Bristol (LA-ICP-MS, VG Elemental Plasma Quad 3). The laser system was used in pulse mode with a frequency of 10 Hz and energy of about 0.1–0.15 mJ/pulse. The laser beam was 20 μm wide. The spots for analysis were selected under optical microscope. The NIST 610 and 612 glasses were used as the external standard and the CaO content in minerals as the internal standard for calculations.

Modal proportions were determined by point counting on 8–10 cm^2 thin sections. Mass-balance calculations were performed by the least-squares analysis method (Spear et al., 1982) in an MSExcel worksheet. Normalisation of rock and mineral analyses to primitive mantle and chondrite were made according to McDonough and Sun (1995).

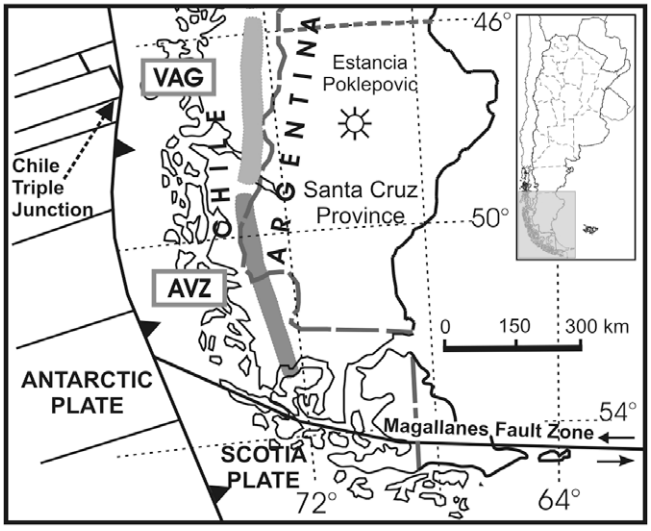

Fig. 1. Simplified map showing the location of Estancia Poklepovic. VAG: Volcanic Arc Gap, AVZ: Austral Volcanic Zone (modified from Bjerg et al. (2005)).

4. Petrographic analysis

A suite of 300 xenoliths was collected from Estancia Poklepovic (48°34′S, 70°10′W) in Santa Cruz province, Argentina (Fig. 1). The xenoliths, with sizes ranging between 10 and 60 cm in diameter (smaller xenoliths, up to 1 cm, were found in the alkali basalt lavas), occur as pyroclasts in a cinder cone. They comprise spinel lherzolites (43%), harzburgites (34%) and wehrlites (21%). The dominant texture (classification of Mercier and Nicolas, 1975) is protogranular to porphyroclastic followed by protogranular and porphyroclastic to equigranular. Porphyroclastic and equigranular, both tabular and mosaic types are also present.

Harzburgites have 64.3–86.9% olivine, 10.4–37.4% orthopyroxene, up to 4.7% clinopyroxene and 1.7% spinel (sensu lato) modal proportions. Lherzolites have 44.8–79.2% olivine, up to 37.5% orthopyroxene, 37.5% clinopyroxene and 1.9% spinel (sensu lato) modal proportions. The only two xenoliths that bear no glass belong to this group. Wehrlites have 75.3–84.1% olivine, up to 1.2% orthopyroxene, 9.1–19.6% clinopyroxene modal proportions. Spinel (sensu lato) is hardly ever present.

Primary clinopyroxene usually shows a spongy rim constituted by an intergrowth of clinopyroxene and glass. These rims are more conspicuous and thick in wehrlites.

Melt pockets and/or glassy veinlets occur in most of the samples. Melt pockets consist of second generation olivine (ol2), clinopyroxene (cpx2) and spinel (sp2) (± relict amphibole, amph) immersed in a yellowish vesicular glass matrix (Fig. 2). The vesicles are sometimes filled with carbonate. Many melt pockets are rounded but some of them show apophyses, the last ones showing continuity with intergranular glassy veins. The melt pocket assemblage may conform up to 10% of the thin section area. The largest observed melt pocket is 7 × 3.5 mm in size.

Second generation olivine and clinopyroxene occur as subhedral to euhedral crystals up to 250–300 μm in size; olivine can occur as inclusions in clinopyroxene and vice versa. Secondary clinopyroxenes sometimes exhibit irregular (patchy) compositional zoning. Second generation spinel is present as subhedral to euhedral crystals up to 80 μm in size and occur included

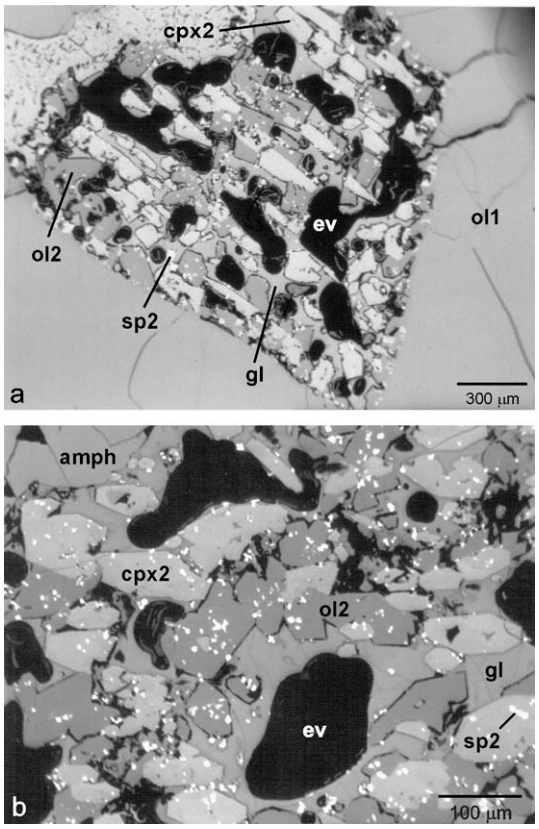

Fig. 2. Backscattered electron images: (a) melt pocket devoid of amphibole, (b) detail of an amphibole-bearing melt pocket. ol1: primary olivine, amph: amphibole, ol2: secondary olivine, cpx2: secondary clinopyroxene, sp2: secondary spinel, gl: glass, ev: empty vesicles.

in cpx2, ol2 or glass. Elongated and spherical empty vesicles (ev) up to 1 mm in diameter are a common feature of the melt pockets. Primary olivine (ol1) shows reaction rims when it is in contact with melt pockets; these rims are more forsteritic and contain trails of sp2, parallel to the boundaries of the melt pockets (Fig. 2a).

Vesicular yellowish glass appears also in veinlets in almost all of the samples, interstitial to or crosscutting primary phases.

Another particular feature of the studied xenoliths is the frequent occurrence of hydrous mineral phases, amphibole, mica or both. Amphibole shows irregular (corroded?) rims and is usually surrounded and/or penetrated by the melt pocket assemblage (ol2 + cpx2 + sp2 + gl). It develops crystals up to 2 mm in size, amounting up to 3% of the modal proportion, regardless of the rock type. In some samples second generation mineral phases crystallise following amphibol cleavage, constituting trails whose central portion is occupied by second generation spinel grains. The last ones are in turn included in second generation clinopyroxene or olivine grains separated by interstitial glass.

Mica occurs as subhedral crystals (up to 1.5 mm) in direct contact with primary phases although sometimes surrounded by gl + ol2 + sp2. This hydrous phase is found mainly in wehrlites but it is also present in lherzolites and harzburgites amounting up to 0.7% modal proportion.

Carbonate fills glass vesicles in melt pockets and veinlets. It has also been recognised conforming veinlets that crosscut primary phases and melt pockets, in the last case also cutting through relict amphibole crystals. In Fig. 3 a fracture cutting through secondary olivine, glass and relict amphibole is filled up with carbonate. Notice that the amphibole and secondary olivine crystals are split apart by this carbonate-filled fracture.

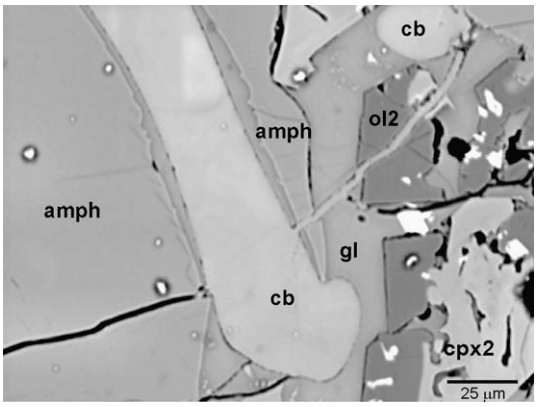

Fig. 3. Backscattered electron image of carbonate-filled fracture cutting trough and displacing secondary olivine, amphibole and glass. amph: amphibole, ol2: secondary olivine, cpx2: secondary clinopyroxene, gl: glass, cb: carbonate.

Apatite has been recognised in several xenolith samples, where it occurs as small subhedral to anhedral crystals (150 μm) and films associated to glass and carbonate veins.

Sulphides are present as very thin veinlets (10 μm wide) along grain boundaries and as droplets included in silicates and glass.

5. Geochemistry

5.1. Bulk rock

5.1.1. Major and trace elements

Representative chemical analyses of peridotite xenoliths from Estancia Poklepovic are given in Table 1. Silica concentration varies between 41.4 and 46.7 wt%. The magnesium number (mg#, Mg/(Mg + Fe) × 100, atomic proportions) ranges between 87.6 and 91.2 increasing from wehrlites to harzburgites. CaO content varies between 0.5 wt% in spinel harzburgites and 4.3 wt% in wehrlites, which is in good agreement with the increase of clinopyroxene modal proportions.

All the chondrite-normalised patterns show LREE enrichment (Fig. 4) with La/Yb_N ratios between 5 and 16. In melt pocket-bearing samples, REE abundances are higher than in chondrites, displaying slight convex-downward patterns.

Compared to concentrations in primitive mantle, the contents of K, Sr and Nb are higher in samples with melt pockets. The primitive mantle-normalised patterns show moderate Ti negative anomalies in these samples, whereas in samples devoid of melt pockets Zr shows negative anomalies.

5.2. Mineral and glass chemistry

5.2.1. Major elements

5.2.1.1. Olivine. Primary olivines show a range of compositions from Fo_{89} to $Fo_{92.0}$ (ol1, Table 2). Second generation olivines (ol2, Table 3) are generally richer in MgO than the primary olivines with compositions ranging from Fo_{92} to Fo_{94}. Second generation olivines are characterised by relatively high CaO concentrations (up to 0.42 wt%), whereas the primary olivines typically have contents of up to 0.07 wt%.

5.2.1.2. Orthopyroxene. Orthopyroxene composition varies from $En_{89.8}Fs_{8.8}Wo_{1.4}$ to $En_{91.2}Fs_{7.5}Wo_{1.3}$ (opx, Table 2). Individual orthopyroxene grains are compositionally homogeneous. In general, orthopyroxenes from wehrlites have lower Al_2O_3 and higher FeO contents than those of lherzolites and harzburgites.

Table 1
Major (wt% oxides) and trace element (ppm) analyses of xenoliths from Estancia Poklepovic.

Sample	dub24	dub10	dub1g	dub80	dub2g	dub27
Rock type	Sp-harzburgite	Sp-lherzolite	Sp-lherzolite	Lherzolite	Wehrlite	Wehrlite
XRF (wt%)						
SiO_2	44.69	44.65	44.88	44.83	41.46	43.20
TiO_2	0.08	0.08	0.11	0.05	0.22	0.12
Al_2O_3	0.95	1.80	1.62	1.57	1.37	1.40
FeO[a]	7.77	8.12	8.34	7.68	10.26	8.67
MnO	0.12	0.13	0.12	0.13	0.15	0.15
MgO	44.99	43.07	42.16	44.30	40.97	42.14
CaO	0.51	1.27	1.25	1.91	4.30	3.39
Na_2O	0.10	0.26	0.16	0.28	0.51	0.50
K_2O	0.12	0.15	0.16	0.07	0.23	0.17
P_2O_5	0.10	0.05	0.04	0.04	0.07	0.05
Total	99.44	99.57	98.84	100.86	99.54	99.79
mg#	91.17	90.44	90.01	91.14	87.68	89.66
XRF + ICPMS (ppm)						
Nb	2	3	0.4	16	17	10
Zr	5	4	b.d.l.	b.d.l.	30	39
Sr	19	43	21	60	85	84
Zn	57	61	57	75	89	75
Ni	2350	2104	2090	2048	2090	2122
Co	113	105	119	113	107	101
Cr	3599	2594	2890	2658	2940	3237
V	35	48	51	27	57	57
Sc	7	11	10	10	11	13
Y	0.9	1.6	1.5	2.3	2.9	3.2
La	0.81	0.91	1.93	1.54	2.58	3.84
Ce	1.51	2.96	2.43	5.14	7.69	9.93
Pr	0.31	0.50	0.39	0.80	1.19	1.38
Nd	1.40	2.30	1.55	3.61	5.39	5.94
Sm	0.29	0.53	0.34	0.86	1.31	1.40
Eu	0.10	0.18	0.13	0.27	0.45	0.48
Gd	0.27	0.50	0.34	0.83	1.25	1.48
Tb	0.03	0.07	0.04	0.11	0.16	0.18
Dy	0.16	0.33	0.24	0.52	0.72	0.84
Ho	0.03	0.06	0.04	0.09	0.11	0.13
Er	0.07	0.16	0.11	0.23	0.26	0.29
Tm	0.01	0.02	0.01	0.03	0.03	0.03
Yb	0.05	0.13	0.09	0.17	0.16	0.17
Lu	0.01	0.02	0.01	0.02	0.02	0.02

[a] Total iron as FeO, b.d.l.: below detection limit.

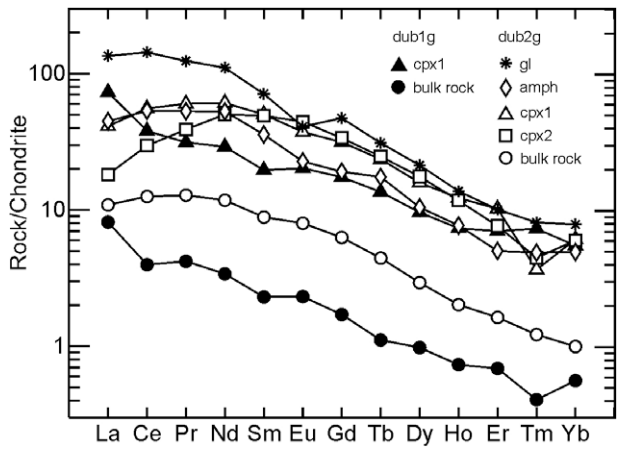

Fig. 4. Chondrite-normalised REE patterns of clinopyroxenes, amphibole, glass and bulk rock. Chondrite normalising values from McDonough and Sun (1995). dub1g: anhydrous melt pocket free spinel lherzolite, dub2g: amphibole and melt pocket-bearing wehrlite.

5.2.1.3. Clinopyroxene. Primary clinopyroxenes are Cr-rich diopsides with compositions varying from $En_{51.0}Fs_{4.2}Wo_{44.8}$ to $En_{51.6}Fs_{5.2}Wo_{43.6}$ (cpx1, Table 2). Second generation clinopyroxenes from the melt pockets (cpx2, Table 3) have highly variable compositions with higher Al_2O_3, Cr_2O_3, TiO_2 and lower Na_2O contents than the primary clinopyroxenes. Primary clinopyroxenes in the hydrous peridotites have higher average Na_2O (ca. 2.5 wt%) than those of the anhydrous peridotites (<1.50 wt% Na_2O). Second generation clinopyroxenes from the melt pockets and from the spongy rims have higher Al_2O_3, Cr_2O_3, TiO_2 and lower Na_2O contents than the primary clinopyroxenes.

5.2.1.4. Spinel. In lherzolites and harzburgites primary Cr-spinels have chromium numbers (cr#, Cr/(Cr + Al) × 100, atomic proportions) ranging from 0.29 to 0.32 (sp1, Table 2) whereas second generation Cr-spinels (sp2, Table 3) have a wider compositional range (cr# = 0.20–0.50). In some samples, secondary spinels show oscillatory zonation with cr# = 0.35 in core and rim and cr# = 0.29 in the intermediate zone between the last two. In general, second generation Cr-spinels have higher TiO_2 contents than the primary ones. Primary spinels are absent in wehrlites.

5.2.1.5. Amphibole. Most of the amphiboles are pargasites (classification of Mogessie et al., 2004) with high contents of Cr_2O_3 (1.7–3 wt%), Na_2O (3.4–4.6 wt%) and K_2O (~1.3 wt% except in dub40 ~0.6 wt%) and relatively low TiO_2 (<2.2 wt%) (Tables 4 and 6). Mg-hastingsite occurs in sample dub24 (Table 4), showing up to 3.5 wt% TiO_2.

5.2.1.6. Mica. Analysed mica crystals belong to the phlogopite group (Table 4). Microprobe analyses show no significant

Table 2
Microprobe analyses of representative primary phases (wt% oxides).

Sample	dub40	dub1g	dub80	dub110	dub2g	dub27
Rock type	Sp-harzburgite	Sp-lherzolite	Lherzolite	Lherzolite	Wehrlite	Wehrlite
ol1						
SiO_2	41.14	41.50	40.41	40.88	40.50	40.40
TiO_2	<0.02	<0.02	<0.02	<0.02	<0.02	<0.02
Al_2O_3	<0.03	<0.03	<0.03	<0.03	<0.03	<0.03
Cr_2O_3	<0.02	0.30	<0.02	0.04	<0.02	0.03
FeO[a]	8.03	8.80	8.89	9.49	10.40	10.10
MnO	0.17	0.13	0.16	0.16	0.17	0.16
MgO	51.81	49.90	51.12	50.32	48.60	50.55
NiO	0.38	0.43	0.35	0.31	0.33	0.35
CaO	0.05	0.06	0.06	0.06	0.07	0.05
Total	101.61	100.89	101.06	101.35	100.11	101.69
Fo[b]	92	91	91	90	89	90
opx						
SiO_2	55.92	56.30	55.50	55.43	56.20	55.40
TiO_2	0.02	0.14	0.03	0.08	0.12	0.06
Al_2O_3	3.54	3.10	2.83	3.40	2.24	2.28
Cr_2O_3	0.65	0.61	0.59	0.51	0.53	0.55
FeO[a]	5.10	5.70	5.62	5.92	6.60	6.33
MnO	0.14	0.10	0.15	0.17	0.15	0.16
MgO	34.92	33.50	35.09	33.99	33.70	34.73
NiO	0.08	0.11	0.08	0.11	0.07	0.06
CaO	0.67	0.73	0.65	0.76	0.79	0.72
Na_2O	0.13	0.13	0.13	0.24	0.16	0.21
Total	101.17	100.46	100.68	100.63	100.56	100.52
En	91.3	90.0	90.6	89.8	88.8	89.5
Fs	7.5	8.6	8.2	8.8	9.7	9.2
Wo	1.3	1.4	1.2	1.4	1.5	1.3
cpx1						
SiO_2	53.13	52.80	52.45	52.91	53.50	53.48
TiO_2	0.04	0.42	0.05	0.14	0.37	0.19
Al_2O_3	5.77	5.00	5.21	5.96	4.10	5.01
Cr_2O_3	1.69	1.44	1.83	1.67	1.80	1.81
FeO[a]	2.29	2.80	2.61	2.80	3.30	3.08
MnO	0.06	0.05	0.08	0.09	0.08	0.08
MgO	15.72	15.50	15.96	15.61	15.70	15.90
NiO	0.07	0.03	0.06	0.05	0.03	0.05
CaO	19.23	19.40	18.92	18.21	18.30	17.86
Na_2O	2.26	1.87	2.17	2.56	2.25	2.50
Total	100.25	99.36	99.34	100.00	99.43	99.97
En	51.0	50.0	51.5	51.6	51.1	52.2
Fs	4.2	5.0	4.7	5.2	6.1	5.7
Wo	44.8	45.0	43.8	43.2	42.8	42.1
sp1			dub10			
SiO_2	0.07	0.05	0.06			
TiO_2	0.04	0.40	0.06			
Al_2O_3	41.05	37.80	39.80			
Cr_2O_3	28.34	28.50	26.50			
FeO[a]	10.45	14.30	15.02			
MnO	0.09	0.08	0.06			
MgO	19.86	17.70	17.90			
NiO	0.28	0.25	0.26			
CaO	0.02	0.02	0.04			
Total	100.22	99.50	100.12			
cr#	0.32	0.32	0.29			

[a] Total iron as FeO.

compositional variations. The average mg# is 86.9, TiO_2 and Cr_2O_3 reach up to 6 and 2 wt%, respectively. Furthermore, phlogopite contains significant amounts of NiO (up to 0.24 wt%).

5.2.1.7. Carbonate. Carbonates are MgO poor calcites (1.55–2.20 wt% MgO). The FeO content ranges from 0.08 to 0.13 wt%; all other elements are below the detection limit.

5.2.1.8. Sulphides. Minor amounts of very fine-grained sulphides are present in several samples. They comprise monosulphide solid-solution (MSS), pentlandite, pyrrhotite and a Cu-rich phase. The chemical composition of the MSS is similar to the Fe_9S_{10}-type pyrrhotite composition. The concentration of Cu in pentlandite ranges from detection limit (0.02 wt%) up to 4.1 wt%, whereas the Co content varies from 0.20 to −0.44 wt%. Pentlandite contains 24.5–38.4 wt% Ni.

5.2.1.9. Glass. Glass in melt pockets and veinlets shows a wide compositional range (Table 3). The SiO_2 content varies between 48.8 and 55 wt% and CaO increases with decreasing SiO_2. Total alkalis reach 12 wt%, Na_2O ranging between 5 and 9 wt% while K_2O varies between 1 and −3 wt%. TiO_2 content is low (<3.0 wt%); the highest measured contents of TiO_2 are those of glass in wehrlites (samples dub27 and dub126).

Compared to the previous glasses, those associated with reaction zones involving primary pyroxenes show higher SiO_2 and lower Al_2O_3 and CaO abundances. This is the case of glasses related to fine-grained olivine-clinopyroxene intergrowths

Table 3
Microprobe analyses (wt% oxides) of representative secondary mineral phases (ol2, cpx2 and sp2) and glass (gl). WRA: melt pocket with relict amphibole, NRA: melt pocket devoid of relict amphibole.

Sample	dub40		dub80		dub110		dub2g		dub27	
Rock type	Sp-harzburgite		Lherzolite		Lherzolite		Wehrlite		Wehrlite	
	WRA	NRA	WRA	NRA	WRA	NRA	WRA	NRA	WRA	NRA
ol2										
SiO_2	41.64	41.74	40.77	41.33	40.93	40.94	41.40	41.13	41.61	41.29
TiO_2	0.00	0.02	0.00	0.00	0.01	0.02	<0.02	0.04	0.00	0.03
Al_2O_3	0.04	0.04	0.04	0.04	0.02	0.05	<0.02	0.04	0.03	0.04
Cr_2O_3	0.10	0.09	0.10	0.13	0.06	0.07	<0.02	0.17	0.09	0.12
FeO[a]	4.80	4.90	8.01	7.00	6.77	7.23	7.10	5.99	5.35	7.46
MnO	0.09	0.10	0.13	0.14	0.12	0.10	0.01	0.12	0.10	0.14
MgO	54.04	54.21	51.97	53.04	52.86	52.18	51.10	52.14	54.04	52.56
NiO	0.32	0.43	0.31	0.32	0.34	0.37	0.33	0.36	0.34	0.34
CaO	0.20	0.32	0.15	0.26	0.20	0.17	0.42	0.33	0.34	0.18
Total	101.26	101.88	101.48	102.29	101.33	101.17	100.49	100.33	101.91	102.19
Fo	95	95	92	93	93	93	93	94	94	93
cpx2										
SiO_2	47.22	47.75	48.41	50.91	47.34	48.58	47.50	48.33	49.55	48.95
TiO_2	0.67	0.59	0.52	0.40	1.09	1.33	2.48	1.96	1.08	1.27
Al_2O_3	8.54	8.22	7.01	5.07	9.61	6.48	6.40	5.78	4.32	6.07
Cr_2O_3	3.22	3.36	3.00	2.18	2.88	2.02	3.20	2.68	2.62	2.54
FeO[a]	2.00	1.81	2.51	2.56	2.33	2.79	2.70	2.90	2.48	2.67
MnO	0.06	0.03	0.05	0.08	0.04	0.05	0.02	0.06	0.06	0.07
MgO	14.68	14.79	15.29	17.08	14.50	15.57	14.50	14.78	16.62	15.38
NiO	0.01	0.03	0.08	0.05	0.05	0.02	0.05	0.04	0.02	0.07
CaO	22.82	22.48	22.81	21.31	20.89	22.28	22.70	22.70	22.38	22.36
Na_2O	0.61	0.63	0.62	0.73	1.28	0.71	0.74	0.88	0.50	0.81
Total	99.84	99.68	100.31	100.38	100.03	99.85	100.15	100.12	99.65	100.21
En	45.6	0.5	46.2	50.5	44.9	45.6	44.8	45.2	48.7	46.7
Fs	3.5	0.0	4.3	4.2	5.2	3.5	4.6	4.9	4.1	4.5
Wo	50.9	0.5	49.5	45.3	49.8	50.9	50.6	49.9	47.2	48.8
sp2										
SiO_2	0.07	0.06	0.08	0.10	0.55	0.14	0.12	0.12	0.07	0.11
TiO_2	0.21	0.25	0.35	0.24	0.75	0.66	1.01	1.77	0.91	0.59
Al_2O_3	38.61	38.80	36.29	42.28	35.82	37.41	31.18	23.35	31.93	41.96
Cr_2O_3	29.54	29.54	31.59	25.78	30.47	30.40	31.64	38.72	33.97	25.23
FeO[a]	9.16	9.23	13.00	11.58	10.83	11.26	15.41	16.02	12.93	11.82
MnO	0.06	0.05	0.07	0.09	0.02	0.03	0.00	0.00	0.07	0.10
MgO	21.17	21.27	19.22	20.07	20.11	19.48	17.22	16.53	19.87	20.30
NiO	0.21	0.31	0.25	0.28	0.23	0.31	0.23	0.22	0.23	0.29
CaO	0.02	0.07	0.04	0.04	0.30	0.20	0.13	0.46	0.05	0.03
Na_2O	0.01	0.02	0.00	0.03	0.04	0.02	0.01	0.00	0.00	0.01
K_2O	0.00	0.02	0.01	0.00	0.06	0.01	0.02	0.02	0.00	0.00
Total	99.08	99.62	100.92	100.49	99.19	99.91	97.01	97.22	100.04	100.43
cr#	0.34	0.34	0.37	0.3	0.2	0.35	0.38	0.49	0.41	0.29
gl										
SiO_2	48.86	51.07	51.39	52.31	49.26	49.96	51.30	51.33	50.67	52.15
TiO_2	0.55	0.60	0.60	0.72	1.39	1.54	3.00	3.13	1.73	1.90
Al_2O_3	21.73	23.09	22.87	21.29	21.84	21.29	20.40	20.17	22.41	22.29
Cr_2O_3	0.04	0.03	0.05	<0.02	0.03	0.02	<0.02	0.10	0.06	0.06
FeO[a]	2.70	2.48	3.23	3.47	3.13	3.39	3.50	3.70	3.14	3.45
MnO	0.05	0.04	0.06	0.06	0.07	0.07	0.10	0.06	0.07	0.08
MgO	5.37	4.17	3.08	2.86	3.93	4.08	3.70	3.84	2.79	2.07
CaO	9.80	8.83	8.28	9.17	9.10	7.89	7.90	8.01	5.88	7.01
Na_2O	7.08	7.31	6.74	6.68	7.05	6.81	6.10	5.74	8.53	8.64
K_2O	1.08	1.11	1.88	1.63	2.46	2.60	2.50	2.53	2.82	1.39
Total	97.30	98.74	98.20	98.23	98.27	97.64	98.66	98.62	98.09	99.05
$Na_2O + K_2O$	8.16	8.42	8.62	8.31	9.51	9.40	8.60	8.27	11.35	10.03

[a] Total iron as FeO.

located at the borders of some orthopyroxene grains displaying reaction rims, and those included in the clinopyroxene spongy rims.

5.2.2. Trace elements

5.2.2.1. Clinopyroxene. Representative trace element analyses of clinopyroxene are given in Table 5. Clinopyroxenes from melt pocket-bearing peridotites have convex-upwards chondrite-normalised REE patterns (Fig. 4). In comparison with primary clinopyroxenes, the second generation clinopyroxenes are less enriched in LREE. Their La/Yb_N ratios range from 2.5 to 4.5, significantly lower than the 6.2–8.3 range in the primary clinopyroxenes. Clinopyroxenes from anhydrous melt-free peridotites show strongly enriched LREE-patterns ($La/Yb_N = 13.4$).

The incompatible elements in clinopyroxenes show complex primitive mantle-normalised patterns. The majority of the primary clinopyroxenes have strong negative Ti anomalies, while they these anomalies are weaker in the second generation clinopyroxenes. All second generation clinopyroxenes display high and variable Nb concentrations, ranging from 1× to 20× primitive mantle concentrations.

5.2.2.2. Amphibole and mica. Representative trace element analyses of amphibole and mica are given in Table 5. Amphibole shows

Table 4
Representative amphibole and mica microprobe analyses (wt% oxides).

	Amphibole			Mica		
Sample	dub24	dub18	dub2g	dub93	dub29	dub18
Rock type	Sp-harzburgite	Wehrlite	Wehrlite	Sp-harzburgite	Lherzolite	Wehrlite
SiO_2	42.70	44.79	44.99	38.47	37.58	38.97
TiO_2	3.50	0.63	2.15	1.54	4.02	1.05
Al_2O_3	13.60	12.96	11.67	15.96	16.67	16.75
Cr_2O_3	1.59	2.26	2.03	1.97	1.03	1.81
FeO[a]	4.50	3.70	4.26	3.21	4.39	3.80
MnO	0.08	0.07	0.04	0.03	0.00	0.00
MgO	17.10	18.74	18.12	23.73	21.44	23.74
NiO	0.03	0.05	0.08	0.19	0.24	0.18
CaO	10.20	9.86	9.80	0.33	0.01	0.03
Na_2O	3.00	3.43	4.26	1.02	0.84	1.02
K_2O	1.69	1.43	1.27	8.40	8.91	9.39
Total	97.99	97.98	98.68	94.85	95.13	96.74

[a] Total iron as FeO.

Table 5
Representative LA-ICP-MS analyses of trace elements (ppm) in clinopyroxenes, amphibole, mica and glass.

	Primary clinopyroxene				Secondary clinopyroxene			Glass			Amphibole		Mica
Sample	dub1g	dub10	dub80	dub2g	dub10	dub80	dub2g	dub10	dub80	dub2g	dub80	dub2g	dub29
Rock type	Sp-lherzolite	Sp-lherzolite	Lherzolite	Wehrlite	Sp-lherzolite	Lherzolite	Wehrlite	Sp-lherzolite	Lherzolite	Wehrlite	Lherzolite	Wehrlite	Lherzolite
Sr	194.00	322.65	335.09	234.00	114.69	100.75	127.00	1424.75	984.89	960.00	502.57	333.00	236.86
Y	9.23	14.12	13.07	11.77	12.97	19.39	11.99	24.44	19.07	15.90	13.22	8.67	10.96
Zr	28.60	46.33	21.44	134.00	31.56	22.10	86.54	127.30	71.85	304.00	28.92	128.00	18.65
Nb	0.97	0.57	1.51	2.34	3.52	5.58	2.20	115.56	371.04	474.00	156.00	205.00	85.81
Cs	b.d.l.	0.00	0.00	b.d.l.	0.00	0.01	b.d.l.	0.01	0.05	b.d.l.	0.01	b.d.l.	4.85
Ba	b.d.l.	0.03	0.21	b.d.l.	4.45	2.46	b.d.l.	150.39	553.08	b.d.l.	258.85	b.d.l.	0.00
La	17.30	10.88	10.99	9.75	3.69	3.63	4.32	35.68	28.45	32.00	12.82	10.59	1.33
Ce	23.30	40.88	47.08	34.01	18.05	22.61	18.21	124.22	94.21	87.90	50.53	32.73	0.92
Pr	2.91	6.11	6.69	5.58	3.84	4.96	3.61	16.28	12.11	11.50	6.80	4.91	0.08
Nd	13.30	27.93	28.91	27.83	19.93	28.55	22.92	64.90	50.96	50.50	30.31	24.14	0.24
Sm	2.90	6.09	6.29	7.43	5.15	9.84	7.25	11.58	8.68	10.50	6.47	5.29	0.03
Eu	1.14	1.93	2.12	2.10	1.84	3.14	2.50	4.02	3.19	2.30	2.20	1.28	2.57
Tb	0.49	0.60	0.60	0.85	0.62	0.94	0.89	0.95	1.09	1.12	0.59	0.63	0.01
Gd	3.47	4.20	4.62	6.27	4.28	7.99	6.72	7.41	8.09	9.37	4.69	3.80	0.06
Dy	2.36	3.22	3.31	3.90	3.12	4.21	4.33	5.27	5.65	5.24	2.93	2.57	0.02
Ho	0.40	0.51	0.57	0.67	0.50	0.85	0.64	0.76	1.00	0.75	0.54	0.42	0.00
Er	1.12	1.44	1.21	1.63	1.54	2.06	1.22	1.88	2.27	1.61	1.20	0.80	0.04
Tm	0.18	0.20	0.17	0.09	0.15	0.19	0.11	0.24	0.33	0.20	0.13	0.12	0.01
Yb	0.88	1.35	1.19	0.98	0.75	1.41	0.96	1.96	0.88	1.26	0.93	0.79	0.02
Lu	b.d.l.	0.18	0.14	b.d.l.	0.09	0.05	b.d.l.	0.24	0.39	b.d.l.	0.10	b.d.l.	0.07
Hf	b.d.l.	0.91	0.18	b.d.l.	0.89	b.d.l.	b.d.l.	2.00	1.09	b.d.l.	0.22	b.d.l.	2.58
Ta	b.d.l.	0.05	0.04	b.d.l.	0.23	0.25	b.d.l.	2.31	4.70	b.d.l.	1.49	b.d.l.	3.56
Th	3.09	0.16	0.41	0.23	0.05	b.d.l.	0.06	0.70	1.13	1.25	0.41	0.15	0.04
U	b.d.l.	0.03	0.22	b.d.l.	0.00	b.d.l.	b.d.l.	0.22	0.50	b.d.l.	0.20	b.d.l.	0.31

b.d.L.: below detection limit.

concave-downwards chondrite-normalised REE patterns which show a steep slope from Nd to Yb (Fig. 4). The La/Nd_N ratio of the amphiboles varies between 0.81 and 1, whereas Nd/Yb_N varies between 9.1 and 13.8. The incompatible element primitive mantle-normalised patterns are characterised by high Nb and Ta concentrations compared to those elements that have similar geochemical behaviour.

Mica has U-shaped chondrite-normalised REE patterns disrupted by a positive Eu anomaly. Except La, Eu and Lu, all of the REE are lower than chondritic abundances. Like the amphiboles, micas show Nb and Ta anomalies when plotted on incompatible element primitive mantle-normalised diagrams.

5.2.2.3. Glass. Representative trace element analyses of glasses are given in Table 5. Glasses have the highest REE contents of all analysed phases (up to 200× chondritic concentration for La and 20 for Yb). Chondrite-normalised patterns make evident a slight decrease from La to Nd (La/Nd_N ratios range from 1 to 1.4) and a more pronounced one from Nd to Yb (Nd/Yb_N ratios between 7 and 40) with a weak negative Eu anomaly (Fig. 4). Nb and Ta are strongly enriched (41–474 and 27.81–43.3 ppm, respectively) in comparison to the elements with similar compatibility (e.g. Th, K and La) giving rise to high positive anomalies in primitive mantle-normalised diagrams (800–1000 × PM).

6. Origin of melt pockets

Several authors have suggested that melt pockets are the result of incongruent breakdown of amphibole (e.g. Ban et al., 2005 and references therein). Textural evidence plus a positive correlation between TiO_2 in amphibole and glass suggest that such a mechanism was responsible for melt pocket generation in the Estancia Poklepovic studied xenoliths.

Mass-balance calculations were performed for several selected xenoliths to test the feasibility of reconstructing the composition of measured amphibole by combining different proportions of the glass and secondary phases present in the melt pockets. These calculations were performed for (a) amphibole-bearing and

Table 6
Representative results of mass-balance calculations.

Sample	dub40					dub93			dub80					dub110				
Rock	Sp-harzburgite					Sp-harzburgite			Lherzolite					Lherzolite				
	WRA			NRA		NRA			WRA			NRA		WRA			NRA	
	m.a.	c.a.	res.	c.a.	res.	m.a.	c.a.	res.	m.a.	c.a.	res.	c.a.	res.	m.a.	c.a.	res.	c.a.	res.
SiO_2	44.00	45.09	0.03	45.25	−0.13	45.53	46.8	−0.09	43.76	45.17	−0.21	45.16	−0.20	43.40	44.82	−0.06	44.98	−0.22
TiO_2	0.39	0.44	−0.04	0.44	−0.04	1.234	1.001	0.265	0.49	0.42	0.08	0.43	0.06	0.94	0.97	0.00	1.11	−0.14
Al_2O_3	14.53	14.99	−0.09	14.85	0.05	11.48	11.69	0.089	13.73	13.83	0.28	13.88	0.23	13.92	14.26	0.10	13.97	0.38
Cr_2O_3	2.30	2.19	0.16	2.50	−0.14	2.879	3.129	−0.175	2.43	2.64	−0.14	2.72	−0.22	2.11	2.23	−0.05	2.52	−0.35
FeO^*	3.16	3.36	−0.12	3.21	0.03	3.678	3.492	0.281	3.72	4.71	−0.88	4.62	−0.80	3.68	4.12	−0.33	4.61	−0.81
MnO	0.04	0.06	−0.02	0.05	−0.01	0.05	0.048	0.004	0.05	0.07	−0.02	0.09	−0.04	0.08	0.07	0.01	0.07	0.02
MgO	18.74	19.23	−0.01	19.12	0.10	18.53	18.97	0.039	18.70	18.91	0.30	18.95	0.26	18.37	18.86	0.09	18.66	0.28
CaO	9.91	10.19	−0.03	9.95	0.21	9.214	9.307	0.145	9.89	9.90	0.26	9.85	0.31	9.65	9.89	0.07	9.66	0.30
Na_2O	3.88	3.79	0.19	3.53	0.45	3.552	3.267	0.377	3.56	3.08	0.58	3.04	0.62	3.49	3.57	0.03	3.33	0.27
K_2O	0.58	0.56	0.03	0.52	0.08	1.333	1.833	-0.465	1.01	0.81	0.22	0.69	0.34	1.31	1.13	0.22	1.21	0.14
Total	97.53					97.6			97.46					96.95				
Σr^2			0.09		0.30			0.58			1.47		1.45			0.18		1.25
Phase proportions	cpx2	22.28		25.80			31.55			27.62		27.75			27.14		26.74	
	ol2	22.70		22.88			21.58			23.94		21.88			23.29		21.93	
	sp2	4.80		5.37			5.39			5.61		8.14			4.61		6.41	
	gl	50.13		45.37			41.01			42.37		41.66			44.89		45.04	

Sample	dub18			dub27					dub126				
Rock	Wehrlite			Wehrlite					Wehrlite				
	NRA			WRA			NRA		WRA			NRA	
	m.a.	c.a.	res.	m.a.	c.a.	res.	c.a.	res.	m.a.	c.a.	res.	c.a.	res.
SiO_2	44.79	45.83	−0.067	44.56	45.69	−0.16	45.52	0.01	44.85	46.02	−0.01	46.15	−0.21
TiO_2	0.627	0.581	0.06	1.294	1.116	0.21	1.18	0.14	1.748	1.72	0.07	1.41	0.33
Al_2O_3	12.96	13.07	0.171	12.56	12.58	0.254	12.86	−0.022	12.12	12.4	0.029	11.83	0.303
Cr_2O_3	2.26	2.489	−0.179	2.245	2.689	−0.39	2.13	0.17	1.481	1.368	0.151	2.061	−0.331
FeO^*	3.701	3.973	−0.191	4.1	3.941	0.25	4.55	−0.361	4.766	5.27	−0.38	5.22	−0.28
MnO	0.07	0.057	0.015	0.048	0.071	−0.02	0.09	−0.04	0.059	0.09	−0.03	0.10	−0.02
MgO	18.74	19.08	0.073	18.61	18.92	0.10	18.98	0.04	18.13	18.54	0.07	18.45	0.21
CaO	9.86	9.983	0.093	9.51	9.479	0.24	9.75	−0.03	9.446	9.70	−0.01	9.46	0.29
Na_2O	3.425	3.693	−0.193	3.579	3.776	−0.12	3.67	−0.02	3.453	3.46	0.08	3.38	0.19
K_2O	1.425	1.098	0.358	1.348	1.202	0.18	0.56	0.82	1.409	1.30	0.14	1.13	0.30
Total	97.98			97.94					97.58				
Σr^2			0.29			0.46		0.86			0.21		0.68
Phase proportions	cpx2	29.60					31.03			28.21		30.82	
	ol2	22.07					23.94			23.42		22.20	
	sp2	5.72					5.11			3.14		4.40	
	gl	42.47					39.21			45.13		41.79	

WRA: MP with relict amphibole

NRA: MP without relict amphibole

m.a.: measured amphibole

c.a.: calculated amphibole

res.: residue

cpx2: secondary clinopyroxene

ol2: secondary olivine

sp2: secondary spinel

gl: glass

FeO^*: total iron as FeO

amphibole-free melt pockets from the same xenolith sample, (b) amphibole-free melt pockets of samples where amphibole occurs only as small inclusions in pyroxenes, and (c) amphibole-free melt pockets from xenoliths which have no amphibole at all. In the latest case, amphibole composition from xenoliths of the petrological type was employed. In order to accomplish these calculations, compositions of all involved phases were normalised to 100 wt% (Table 6).

The proposed reaction that relates amphibole and the melt pocket assemblage is:

$$\text{Amph} \rightarrow \text{cpx2} + \text{ol2} + \text{sp2} + \text{melt}$$

In the case of a melt pocket in which relict amphibole is present (an example is WRA from sample dub40, Table 6), the previous reaction can be written as

$$\text{Amph} \rightarrow 0.22\text{cpx2} + 0.22\text{ol2} + 0.05\text{sp2} + 0.5\text{melt}$$

For the same sample (dub40, Table 6) but considering a melt pocket in which relict amphibole is absent (NRA) the previous reaction would be:

$$\text{Amph} \rightarrow 0.26\text{cpx2} + 0.23\text{ol2} + 0.05\text{sp2} + 0.45\text{melt}$$

In the case of a xenolith which has no amphibole in melt pockets but does have it as inclusions in pyroxene (e.g. dub18), the reaction would be (Table 6):

$$\text{Amph} \rightarrow 0.30\text{cpx2} + 0.22\text{ol2} + 0.06\text{sp2} + 0.43\text{melt}$$

In the case of xenoliths which bear no amphibole at all, measured amphibole compositions from other nodules of same rock type and texture were employed for the calculations (e.g. composition of amphibole in melt pockets from dub48 were used in the calculations performed for amphibole-free dub93 xenolith). The reaction can be written as (Table 6):

$$\text{Amph} \rightarrow 0.32\text{cpx2} + 0.22\text{ol2} + 0.05\text{sp2} + 0.41\text{melt}$$

In all cases, the composition of the calculated amphibole is very similar to the measured one, which is also reflected by the low $\sum r^2$ value. Furthermore, the proportions of secondary phases are in good agreement with the proportions revealed by the backscattered electron (BSE) images.

7. Discussion and conclusions

The mantle portions sampled by the alkali volcanism at Estancia Poklepovic were affected by several processes before they reached the surface as xenoliths included in volcanic products.

The studied xenoliths were affected by cryptic and modal metasomatism (Gorring and Kay, 2000; Laurora et al., 2001; Rivalenti et al., 2004a,b; Bjerg et al., 2005). The cryptic metasomatism is evidenced by high bulk LREE contents in samples devoid of melt pockets, glass and hydrous phases (amphibole and/or mica). In this case, the use of the term "cryptic" is not strictly correct since REE are in fact hosted by clinopyroxene. On the other hand, this metasomatism cannot be referred to as "modal" as far as clinopyroxene is a "normal" phase in mantle xenoliths.

The modal metasomatism is evidenced by the occurrence of amphibole, mica, apatite and probably glass. Partition coefficients for REE between amphibole and primary clinopyroxene are consistent with those presented in modern literature (e.g. Chazot et al., 1996 and references therein) which suggests that these two phases are in mutual equilibrium.

Amphibole breakdown, probably caused by decompression melting prior to or during the entrapment of the xenoliths by the host magma, was responsible for melt pocket generation as it is shown by textural evidences and consistent mass-balance calculations. Regarding errors in mass-balance calculations, they can be in part attributed to minor errors inherent to conventional analytical techniques, in this study electron microprobe.

In some samples, the calculated phase proportion of glass appears to be in excess compared to estimations made based on the BSE images. In order to perform these comparisons, mass to volume transformations, based on the density of each phase, were done. One plausible explanation for the above mentioned discrepancy is that a portion of the generated melt was able to migrate out of the melt pockets through the intergranular spaces. This is supported by the chemical similarities between glasses present in melt pockets and network-like veinlets.

The composition of the calculated amphibole in amphibole-free melt pockets is very similar to that measured in amphibole-bearing melt pockets from the same xenolith. This implies that amphibole was totally consumed in the process that produced glass and secondary phases (olivine, clinopyroxene, spinel). The model provides consistent results even for xenoliths that have amphibole as small inclusions in pyroxenes (but not in their melt pockets) and for some which have no amphibole at all. In the last case calculations were performed based on amphibole analyses present in petrographically similar xenoliths.

In some cases, mass-balance calculations show remarkable differences between the calculated amphibole and the measured amphibole compositions. A possible involvement of minor proportions of a reactant phase that left no traces of its presence could be a reasonable explanation in these cases but further work is needed to test this hypothesis.

In chondrite-normalised diagrams, the pattern corresponding to bulk rock parallels that of primary clinopyroxene from the same sample, maybe due to the fact that, in the studied samples, clinopyroxene is the most abundant phase of those that can incorporate REE in their structure. The relative LREE depletion in secondary clinopyroxene probably reflects the increase of incompatibility from Nd to La. This promotes preferential partitioning of LREE into the glass when amphibole becomes unstable.

Compositional inhomogeneity of second generation clinopyroxene and variable Ti Kd in secondary clinopyroxene vs. glass in the same melt pocket support fast nucleation and growth and disequilibrium crystallisation, respectively, reflecting rapid quenching of melt pockets which inhibited mineral equilibration. Calculated equilibrium olivine composition (Roeder and Emslie, 1970) reveal that Fo content of calculated olivine is different from that of the second generation olivine, suggesting disequilibria between melt and second generation olivine. In addition, the fact that glasses are exceptionally fresh indicates that amphibole breakdown took place not long before xenoliths were entrained by the host basalts or during their transport to the surface.

Gorring and Kay (2000) and Laurora et al. (2001) suggested that carbonates associated to the xenoliths from the area of Gobernador Gregores are of mantle origin. In the studied samples, in addition to carbonates filling up bubbles in glass, we recognised calcite veins and carbonate filling interstices and cavities in the primary mineral phases. This fact strongly suggests that at least part of the carbonate present in these xenoliths was introduced by meteoric water percolating the xenoliths. This carbonate was probably provided by upper Oligocene marine sediments which are of widespread occurrence in the area. This would also explain the very common presence of a carbonate crust covering the outer part of both mantle xenoliths and basalt fragments.

Acknowledgements

This work was financed by ANPCYT (Argentina) – Grant BID 1728/OC-AR – PICT 07-11791 and SGCyT-UNS (Argentina) – Grant PGI 24/H066 to EB. PA is grateful to CONICET (Argentina) for a PhD

scholarship. The authors are grateful to F. Costa Rodríguez and D. Gimeno for valuable comments, which helped to improve the article.

References

Aliani, P.A., Bjerg, E.A., Ntaflos, Th., 2004. Evidencias de metasomatismo en el manto sublitosférico de Patagonia. Revista de la Asociación Geológica Argentina 59 (4), 539–555.

Ban, M., Witt-Eickschen, G., Klein, M., Seck, H.A., 2005. The origin of glasses in hydrous mantle xenoliths from the West Eifel, Germany: incongruent break down of amphibole. Contributions to Mineralogy and Petrology 148, 511–523.

Bjerg, E.A., Ntaflos, Th., Kurat, G., Dobosi, G., Labudia, C.H., 2005. The upper mantle beneath Patagonia, Argentina, documented by xenoliths from alkali basalts. Journal of South American Earth Sciences 18 (2), 125–142.

Cande, S.C., Leslie, R.B., 1986. Late Cenozoic tectonics of the Southern Chile Trench. Journal of Geophysical Research 91, 471–496.

Chazot, G., Menzies, M.A., Harte, B., 1996. Silicate glasses in spinel lherzolites from Yemen: origin and chemical compositions. Chemical Geology 134, 159–179.

Coltorti, M., Bonadiman, C., Hinton, R.W., Siena, F., Upton, B.J., 1999. Carbonatite metasomatism of the oceanic upper mantle: evidence from clinopyroxenes and glasses in ultramafic xenoliths of grande comore, Indian Ocean. Journal of Petrology 40, 133–165.

Frey, F.A., Green, D.H., 1974. The mineralogy, geochemistry and origin of lherzolite inclusions in Victorian basanites. Geochimica et Cosmochimica Acta 38, 1023–1059.

Gorring, M.L., Kay, S.M., Zeitler, P.K., Ramos, V.A., Rubiolo, D., Fernandez, M.I., Panza, J.L., 1997. Neogene Patagonian plateau lavas: continental magmas associated with ridge collision at the Chile Triple Junction. Tectonics 16 (1), 1–17.

Gorring, M.L., Kay, S.M., 2000. Carbonatite metasomatised peridotite xenoliths from southern Patagonia: implications for lithospheric processes and Neogene plateau magmatism. Contributions to Mineralogy and Petrology 140, 55–72.

Gorring, M.L., Kay, S.M., 2001. Mantle processes and source of Neogene slab window magmas from Southern Patagonia, Argentina. Journal of Petrology 42, 1067–1094.

Laurora, A., Mazzucchelli, M., Rivalenti, G., Vannucci, R., Zanetti, A., Barbieri, M.A., Cingolani, C.A., 2001. Metasomatism and melting in carbonated peridotite xenoliths from the mantle wedge: the Gobernador Gregores case (southern Patagonia). Journal of Petrology 42 (1), 69–87.

McDonough, W.F., Sun, S.-S., 1995. The composition of the Earth. Chemical Geology 120, 223–253.

Mercier, J.C.C., Nicolas, A., 1975. Textures and fabrics of upper – mantle peridotites as illustrated by xenoliths from basalts. Journal of Petrology 16 (2), 454–487.

Mogessie, A., Ettinger, K., Leake, B.E., 2004. IMA-Amphibole classification chart. <www.minersoc.org>.

Neumann, E.R., Wulff-Pedersen, E., 1997. The origin of highly silicic Glass in mantle xenoliths from the Canary Islands. Journal of Petrology 38, 1513–1539.

Pouchou, J.L., Pichoir, F., 1991. Quantitative analysis of homogeneous or stratified microvolumes applying the model "PAP". In: Heinrich, K.F.J., Newbury, D.E. (Eds.), Electron Probe Quantitation. Plenum Press, New York, pp. 31–75.

Ramos, V.A., Kay, S.M., 1992. Southern Patagonian plateau basalts and deformation: backarc testimony of ridge collisions. Tectonophysics 205, 261–282.

Ramos, V.A., 1999. Plate tectonic setting of the Andean Cordillera. Episodes 22 (3), 183–190.

Rivalenti, G., Zanetti, A., Mazzucchelli, M., Vannucci, R., Cingolani, C.A., 2004a. Equivocal carbonatite markers in the mantle xenoliths of the Patagonia backarc: the Gobernador Gregores case (Santa Cruz Province, Argentina). Contributions to Mineralogy and Petrology 147, 647–670.

Rivalenti, G., Mazzucchelli, M., Laurora, A., Ciuffi, S.I.A., Zanetti, A., Vannucci, R., Cingolani, C.A., 2004b. The backarc mantle lithosphere in Patagonia, South America. Journal of South American Earth Sciences 17, 121–152.

Roeder, P.L., Emslie, R.F., 1970. Olivine-liquid equilibrium. Contributions to Mineralogy and Petrology 29, 275–289.

Spear, F.S., Rumble III, D., Ferry, J.M., 1982. Linear algebraic manipulation of n-dimensional composition space. Reviews in Mineralogy 10, 53–104.

Stern, C.R., Kilian, R., 1996. Role of the subducted slab, mantle wedge and continental crust in the generation of adakites from the Andean Austral Volcanic Zone. Contributions to Mineralogy and Petrology 123, 263–281.

Stern, C.R., 2004. Active Andean volcanism: its geologic and tectonic setting. Revista Geológica de Chile 31 (2), 161–206.

Yaxley, G.M., Kamenetsky, V., 1999. In situ origin for glass in mantle xenoliths from southeastern Australia; insights from trace element compositions of glasses and metasomatic phases. Earth and Planetary Science Letters 172, 97–109.